# Percolation of defective dimers irreversibly deposited on honeycomb and triangular lattices

P. M. Centres and A. J. Ramirez-Pastor*
*Departamento de Física, Instituto de Física Aplicada (INFAP), Universidad Nacional de San Luis-CONICET, Ejército de Los Andes 950, D5700HHW, San Luis, Argentina*

M. C. Gimenez
*Facultad de Matemática, Astronomía, Física y Computación, U.N.C., Córdoba, IFEG-CONICET, Argentina*

(Received 16 September 2018; published 19 November 2018)

The percolation problem of irreversibly deposited dimers on honeycomb and triangular lattices is studied. A dimer is composed of two segments, and occupies two adjacent adsorption sites. Each segment can be either a conductive segment (segment type $A$) or a nonconductive segment (segment type $B$). Three types of dimers are considered: $AA$, $BB$, and $AB$. The connectivity analysis is carried out by accounting only for the conductive segments (segments type $A$), whereas the $B$ segments occupy a site in the lattice but are not taken into account in the percolation study. Different cases were investigated, according to the types of dimers involved in the process. By means of numerical simulations and finite-size scaling techniques, the complete phase diagram separating the percolating from the nonpercolating regions was determined for each considered lattice. The present results are compared with the previous study of deposition of defective dimers on square lattices.

DOI: 10.1103/PhysRevE.98.052121

## I. INTRODUCTION

The study of percolation in systems of hard elongated particles is one of the central problems in statistical mechanics and has been attracting a great deal of interest since long ago [1–15]. In this framework, the dimer is the simplest case of an extended object and, consequently, the percolation problem of irreversibly deposited dimers on a lattice has been extensively studied in the literature [16–19].

From an experimental point of view, numerous studies on molecular adsorption on some kinds of metal surfaces show that the deposition is the initial step and is followed by dissociation. Among them, the oxidation of carbon monoxide [20]; the dissociative chemisorption of $N_2$ on Fe(111) [21], $O_2$ on Pt(111) [22], $O_2$ on Ir(111) [23], etc. In all cases, when the diatomic molecule ($O_2$, $N_2$) dissociates, it is broken into two monomers, each of which occupies a site. The distributions of such dissociated monomers and the structure of the clusters composed by them are important factors in the catalytic processes. Because the dimers are randomly placed on the lattice and randomly dissociate, the dissociative adsorption is a spatial random process and can clearly be modeled by dimer percolation models. In this sense, Gao *et al.* [24] investigated the process of dissociative adsorption of dimers and studied the percolation properties of the dissociated monomers. In the model, an $O_2$ molecule adsorbs onto a pair of neighboring sites and then dissociates. A complete phase diagram separating a percolating from a nonpercolating region was obtained in terms of the concentration of dimers and the dissociation probability.

A model involving the formation of dimers on the surface was also used to describe the nonlinear dependence of transport properties on composition in mixed-alkali ionic conductors [25]. Along the same line, Holloway [26] studied the problem of site percolation on a diamond lattice occupied by a mixture of monatomic and diatomic species. The results allowed us to understand some of the features of the alloys of Ge with group III-V semiconductors.

Two previous articles [27,28], referred to as papers I and II, respectively, were devoted to the study of percolation of heteronuclear dimers irreversibly deposited on square lattices. In paper I, a site percolation model of defective (or heteronuclear) dimers was investigated. The presence of defects was introduced as two kinds of segments composing the dimers: segment type $A$ (conductive segment) and segment type $B$ (nonconductive segment). Each segment occupies one lattice site. Three types of dimers were considered: $AA$, $BB$, and $AB$. The connectivity analysis was carried out by accounting only for the conductive segments (segments type $A$). The model offers a simplified representation of the problem of percolation of defective (nonideal) particles, where the presence of defects in the system is simulated by introducing a mixture of conductive and nonconductive segments. Different cases were studied, according to the sequence of deposition of the particles, the types of dimers involved in the process, and the degree of alignment of the deposited objects. By means of numerical simulations and finite-size scaling analysis, the complete phase diagram separating a percolating from a nonpercolating region was determined for each case.

In paper II, a generalization of the site-bond percolation problem was studied, in which pairs of neighboring sites (site dimers) and bonds were occupied irreversibly, randomly, and independently on homogeneous square surfaces. As in paper I, the dimers were modeled as objects composed by conductive

*To whom all correspondence should be addressed: antorami@unsl.edu.ar

 

(type $A$) and nonconductive (type $B$) segments. Two different criteria were used for the connectivity analysis: the union or the intersection between the conductive segments and the bonds. The corresponding percolation phase diagrams were determined. The aim of this paper is to study percolation of defective dimers on triangular and honeycomb lattices using the same techniques developed in papers I and II.

A site percolation model of linear $k$-mers with defects ($k$-mers containing a fraction of nonconducting defects) on an ideal square lattice was studied by Tarasevich *et al.* [29]. $k$-mer sizes ranging from 2 to 256 were considered. For each size $k$, a critical concentration of defects was found. Above this concentration, percolation is impossible. In the case of $k = 2$ (dimers), the results in Ref. [29] were found to be consistent with those from Ref. [27].

In contrast to the statistic for the simple particles, the degeneracy of arrangements of dimers is strongly influenced by the structure of the lattice space [30]. Because the structure of lattice space plays such a fundamental role in determining the statistics of dimers, it is of interest and of value to inquire how a specific lattice structure influences the main percolation properties of heteronuclear dimers. In this sense, the aim of this work is to study the effect of the lattice structure on the percolation transition occurring in a system of defective dimers. For this purpose, extensive numerical simulations have been performed to study the percolation of dimers composed of segments $A$ and $B$ deposited on triangular and honeycomb lattices. The results obtained are discussed and compared with data from square lattices [27,28].

This paper is organized as follows. The model and simulation scheme used to study the percolation phase transition are described in Sec. II. Results are presented and discussed in Sec. III. Finally, some conclusions are drawn in Sec. IV.

## II. MODEL AND CALCULATION METHOD

We consider the percolation of heteronuclear dimers on triangular and honeycomb lattices. A dimer consists of two segments, and occupies two adjacent sites on the lattice. Thus, a lattice site is occupied by one segment, or is empty. Each segment can be either a conductive segment (segment type $A$) or a nonconductive segment (segment type $B$). Three types of dimers have been considered: $AA$, $BB$, and $AB$ (see Fig. 1); and the percolation analysis is carried out by taking into account only the conductive segments (segments type $A$).

In order to represent the honeycomb and triangular lattices, a one to one mapping from each kind of lattice to a square lattice, with the appropriate connectivity is performed. This correspondence is illustrated in Fig. 1. In the case of honeycomb lattices (connectivity $z = 3$), this structure is not a Bravais lattice and two types of sites [$l$ and $r$, see Fig. 1(a)] can be distinguished. $l$ and $r$ are not equivalent sites. Thus, each $l$ site is connected to three $r$ sites and each $r$ site is connected to three $l$ sites. On the other hand, for the triangular lattice, each site has six neighboring ones ($z = 6$). The two-dimensional square lattice consists on $M = L \times L$ sites for the triangular case and $M = \frac{1}{2}(L \times L)$ sites for the honeycomb case, with periodic boundary conditions.

In the filling process, two different cases have been considered, according to the types of dimers deposited on the lattice:

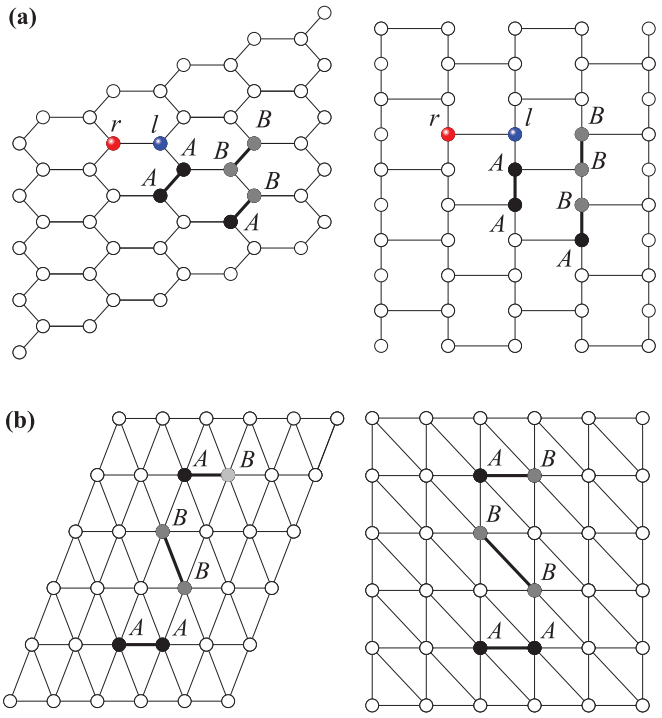


FIG. 1. Heteronuclear dimers deposited on (a) a honeycomb lattice with $L = 10$, and (b) a triangular lattice with $L = 6$. Black circles, gray circles, and open circles represent $A$-dimer units, $B$-dimer units, and empty sites, respectively. The definitions of $r$ and $l$ are given in the text.

*Model I:* Starting from an initially empty lattice, $AB$ and $AA$ dimers are deposited up to a total coverage $\theta_T = \theta_{AB} + \theta_{AA}$ is reached. $\theta_{AB}$ ($\theta_{AA}$) represents the fraction of the lattice covered by $AB$ ($AA$) dimers. Due to the blocking of the lattice by the already randomly deposited objects, the limiting or jamming coverage $\theta_j$ is less than that corresponding to the close packing ($\theta_j < 1$). Consequently, the total site coverage $\theta_T$ ranges from 0 to $\theta_j$. In the case of triangular (honeycomb) lattices, the value of the jamming coverage for the conventional dimer filling problem is $\theta_j = 0.9142(12)$ [31] [$\theta_j = 0.864(7)$ [32]]. In this study, we initially fix the value of $\theta_{AB}$. In a second stage, a fraction $\theta_{AA}$ of $AA$ dimers is deposited on the lattice.[1]

*Model II:* Starting from an initially empty lattice, $BB$ and $AA$ dimers are deposited up to a total coverage $\theta_T = \theta_{BB} + \theta_{AA}$ is reached. As in model I, $\theta_T$ varies between 0 and $\theta_j$. In this case, we initially fix the value of $\theta_{BB}$ and, in a second stage, a fraction $\theta_{AA}$ of $AA$ dimers is deposited on the lattice.

For what follows, it is useful to define $\theta_1$ ($\theta_2$) as the fraction of dimers deposited in a first (second) stage. Thus, $\theta_1 = \theta_{AB}$ and $\theta_2 = \theta_{AA}$ for model I; and $\theta_1 = \theta_{BB}$ and $\theta_2 = \theta_{AA}$ for model II. In both models, the dimers are deposited randomly, sequentially, and irreversibly on the lattice. The procedure is the following:

[1]Equivalent configurations can be obtained by initially depositing all dimers on the lattice up to desirable total concentration $\theta_T = \theta_{AB} + \theta_{AA}$, and then randomly differentiating these dimers on $AB$ and $AA$ types according to their concentration [27,28].

(1) One lattice site $i$ is chosen at random.

(2) If the site $i$ is empty, then one of the $z$ nearest neighbors of $i$ is randomly chosen. $z = 3$ ($z = 6$) for honeycomb (triangular) lattices.

(3) If both sites are unoccupied, a dimer is deposited on those two sites. Otherwise, the attempt is rejected.

(4) Steps 1–3 are repeated until the desired concentrations $(\theta_1, \theta_2)$ are reached or until jamming conditions.

A cluster is a group of occupied sites in such a way that each one of them has at least one occupied nearest neighbor site. The central idea of the percolation theory is based on finding the minimum coverage degree for which at least a cluster extends from one side to the opposite one of the system. This particular value of the coverage degree is named *percolation threshold*. In the present model, given $\theta_1$, we look for the value of $\theta_2 = \theta_{2,c}$ for which percolation occurs, and that value will be our percolation threshold.

The larger the system size to study, the more accurate the values of the threshold obtained [33]. Thus, the finite-size scaling theory gives us the basis to achieve the percolation threshold and the critical exponents of a system. For this purpose, the probability $R = R_L^X(\theta_1, \theta_2)$ that a lattice of linear size $L$ percolates at concentrations $\theta_1$ and $\theta_2$ can be defined [34]:

(i) $R_L^R(\theta_1, \theta_2)$: the probability of finding a rightward percolating cluster, along the $x$ direction (see Fig. 1).

(ii) $R_L^D(\theta_1, \theta_2)$: the probability of finding a downward percolating cluster, along the $y$ direction (see Fig. 1).

(iii) $R_L^U(\theta_1, \theta_2)$: the probability of finding a cluster which percolates on any direction.

(iv) $R_L^I(\theta_1, \theta_2)$: the probability of finding a cluster which percolates in both (mutually perpendicular) directions.

(v) $R_L^A(\theta_1, \theta_2) = \frac{1}{2}[R_L^U(\theta_1, \theta_2) + R_L^I(\theta_1, \theta_2)]$.

In the simulations, each run consists of the following steps: (a) the construction of the lattice for the desired fractions $(\theta_1, \theta_2)$, according to the scheme mentioned before, and (b) the cluster analysis by using the Hoshen and Kopelman algorithm [35]. In the latter step, the size of largest cluster $S_L$ is determined, as well as the existence of a percolating island.

$n$ runs of such two steps are carried out for obtaining the number $m^X$ ($X = I, U, A$) of them for which a percolating cluster is found. Then, $R_L^X(\theta_1, \theta_2) = m^X/n$ is defined, and the procedure is repeated for a fixed value of $\theta_1$ and different values of $\theta_2$. For each lattice, each model and each pair $(\theta_1, \theta_2)$, a set of $n = 100\,000$ independent samples is numerically prepared.

The percolation threshold can be estimated from the curves of $R_L^X(\theta_2)$ for the different values of $L$ [36–38]. Additionally, in order to determine the universality class which this problem belongs to, the critical exponents $\nu$, $\beta$, and $\gamma$ have been calculated. For this purpose, the percolation order parameter $P$ and its corresponding susceptibility $\chi$ have been obtained [39,40]. Thus,

$$P = \frac{\langle S_L \rangle}{M} \tag{1}$$

and

$$\chi = \frac{\langle S_L^2 \rangle - \langle S_L \rangle^2}{M}, \tag{2}$$

where $S_L$ represents the size of the largest cluster and $\langle \ldots \rangle$ means an average over simulation runs.

## III. RESULTS AND DISCUSSION

### A. Percolation and phase diagrams

The curves of probability $R_L^U$, $R_L^I$, and $R_L^A$ are reported in Fig. 2 for two typical cases: (a) model I, honeycomb lattice and $\theta_1 = 0.20$; and (b) model II, triangular lattice and $\theta_1 = 0.32$. In both cases, the simulations were performed for lattice sizes of $L = 128$, 192, 256, 320, and 384. For clarity, two sizes are shown in Fig. 2: $L = 128$ (squares) and $L = 384$ (triangles).

The following observations can be done from the data presented in Fig. 2: (a) the behavior of the probability curves tends to be more abrupt for increasing values of $L$; it agrees with the percolation theory [36], i.e., these curves are expected to approach a step function in the thermodynamic limit ($L \to \infty$) at $\theta_2 = \theta_{2,c}$; (b) curves cross each other in a point $R^{X^*}$,

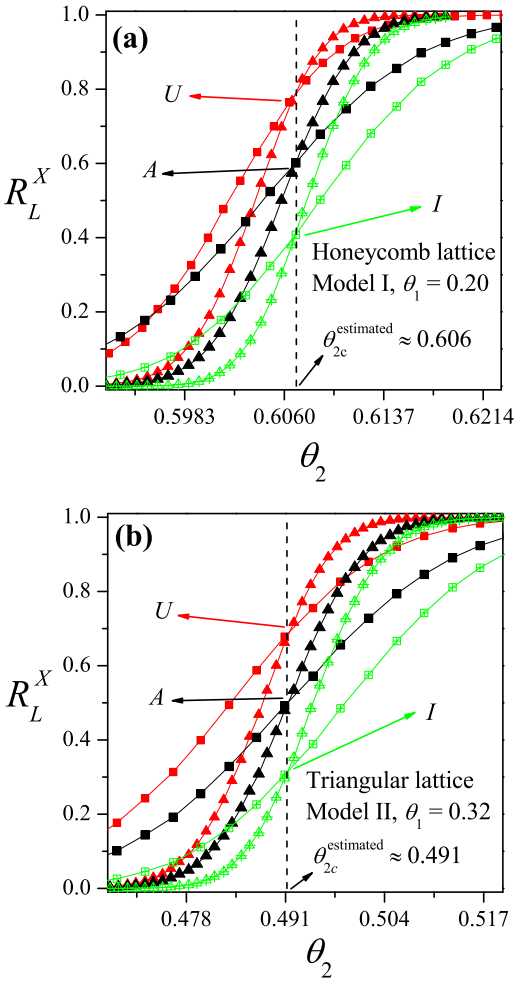


FIG. 2. Probability of percolation $R_L^X$ ($X = I$, $U$, and $A$, as defined in Sec. II) as a function of $\theta_2$ for two lattice sizes: $L = 128$ (squares) and $L = 384$ (triangles). Two cases are shown: (a) model I, honeycomb lattice, $\theta_1 = 0.20$; and (b) model II, triangular lattice, $\theta_1 = 0.32$. The vertical dashed line denotes the percolation threshold in the thermodynamic limit.

which depends on the criterion $X$ used; and (c) those points are located at very well defined interval in the $\theta$ axis, which allow us to have an early estimation of the critical percolation threshold [41]. In the case of Fig. 2, $\theta_{2,c}^{\text{estimated}} \approx 0.606$ in part (a) and $\theta_{2,c}^{\text{estimated}} \approx 0.491$ in part (b). These values are different from those of the percolation threshold for homogeneous dimers on honeycomb lattices $\theta_c = 0.6905(6)$ [42] and triangular lattices $\theta_c = 0.4876(5)$ [31].

The finite-size scaling theory can be used to obtain more accurate values of the percolation thresholds [33,36]. To do this, first it is convenient to fit the curves of probability with some function through the least-squares method so that they can be expressed as a continuous function of $\theta_2$. The fitting curve used is the *error function* because $dR_L^X(\theta_1,\theta_2)/d\theta_2$ is expected to behave like the Gaussian distribution near the peak. This assumption is good enough to obtain the parameters that are needed to apply finite-size scaling theory [4,36]:

$$\frac{dR_L^X(\theta_1,\theta_2)}{d\theta_2} = \frac{1}{\sqrt{2\pi}\,\Delta_L^X} \exp\left\{-\frac{1}{2}\left[\frac{\theta_2 - \theta_{2,c}^X(L)}{\Delta_L^X}\right]^2\right\}, \quad (3)$$

where $\theta_{2,c}(L)$ is the concentration at which the slope of $R_L^X(\theta_1,\theta_2)$ is the largest and $\Delta_L^X$ is the standard deviation from $\theta_{2,c}(L)$. For large systems $L \to \infty$, these thresholds converge to a unique value according to the scaling behavior [36]

$$\theta_{2,c}^X(L) = \theta_{2,c}^X(\infty) + A^X L^{-1/\nu}, \quad (4)$$

where $A^X$ is a nonuniversal constant and $\nu$ is the critical exponent of the correlation length which has been taken as $\frac{4}{3}$ for this study since, as it will be shown below, our model belongs to the same universality class as random percolation [36].

Figure 3 shows the plots towards the thermodynamic limit of $\theta_{2,c}^{I,A,U}(L)$ according to Eq. (4) for the data corresponding to Fig. 2. From extrapolations it is possible to obtain $\theta_{2,c}^X(\infty)$ for each criteria $I$, $A$, and $U$. The final value is given by $\theta_{2,c} \pm \delta_{2,c}$, where $\delta_{2,c} = \max(|\,\theta_{2,c}^U - \theta_{2,c}^A\,|, |\,\theta_{2,c}^I - \theta_{2,c}^A\,|)$. In Fig. 3, $\theta_{2,c}(\infty) = 0.6069(2)$ for case (a) and $\theta_{2,c}(\infty) = 0.4915(3)$ for case (b). Note that the values obtained in Fig. 3 match, within the statistical errors, with those calculated in Fig. 2. For the rest of the paper, we will denote the percolation threshold by $\theta_{2,c}$ [for simplicity we will drop the symbol "$(\infty)$"].

The procedure shown in Figs. 2 and 3 was repeated for both models (I and II) and different values of $\theta_1$. The results for honeycomb and triangular lattices are shown in Figs. 4(a) and 4(b), respectively. Each figure represents the complete percolation phase diagram corresponding to the deposition of heteronuclear dimers. As mentioned in the previous section, $\theta_1 = \theta_{AB}$ (vertical axis) and $\theta_2 = \theta_{AA}$ (horizontal axis) for model I, and $\theta_1 = \theta_{BB}$ (vertical axis) and $\theta_2 = \theta_{AA}$ (horizontal axis) for model II.

We consider in the first place the phase diagram corresponding to heteronuclear dimers deposited on honeycomb lattices [see Fig. 4(a)]. The solid straight curve accounts for the jamming restriction. This means that the total coverage is always less or equal to $\theta_j = 0.864(7)$ for both models. Then, the region above this curve corresponds to a forbidden area for any combination of dimers. On the other hand, the region

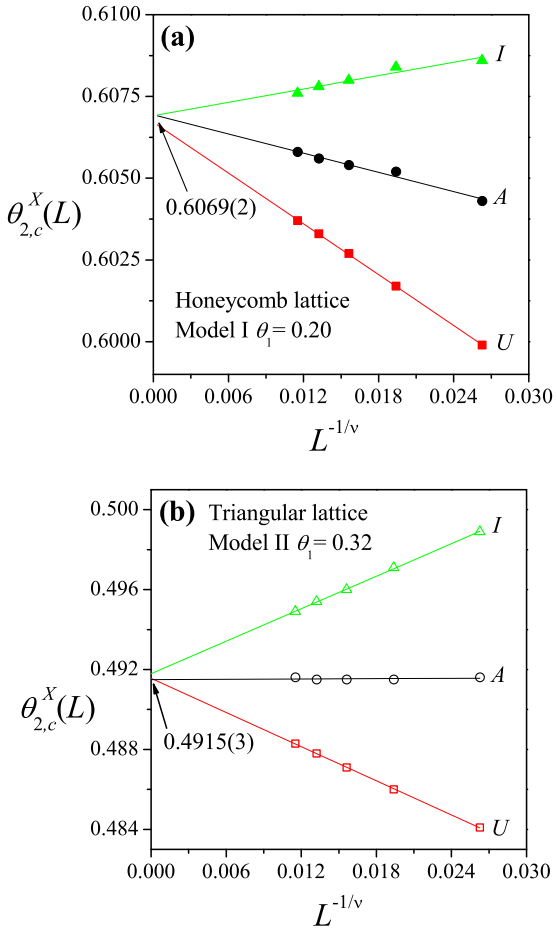


FIG. 3. Extrapolation of $\theta_{2,c}^X(L)$ towards the thermodynamic limit according to the theoretical prediction given by Eq. (4). Triangles, circles, and squares denote the values of $\theta_{2,c}^X(L)$ obtained by using the criteria $I$, $A$, and $U$ (as defined in Sec. II), respectively. Two cases have been considered: (a) model I, honeycomb lattice, $\theta_1 = 0.20$; and (b) model II, triangular lattice, $\theta_1 = 0.32$.

below this curve represents the space of all the allowed values of the total coverage. The curve of solid circles separates the nonpercolating region (on the left) from the percolating region (on the right) for model I. The curve of solid stars separates the nonpercolating region (on the left) from the percolating region (on the right) for model II. Both curves begin at $\theta_2 = 0.6905(6)$. This value represents percolation threshold for homogeneous dimers on honeycomb lattices [42]. To sum up, four regions can be distinguished in the percolation phase diagram. Region 1: forbidden region for models I and II; region 2: nonpercolating region for both models I and II; region 3: percolating region for model I and nonpercolating region for model II [see inset in Fig. 4(a)]; and region 4: percolating region for models I and II.

From Fig. 4(b), it can be seen that the phase diagram for triangular lattices has a similar pattern to the phase diagram for honeycomb lattices. The solid straight curve indicates the jamming condition, i.e., the total coverage is always less or equal to $\theta_j = 0.9142(12)$ for both models. The curve of solid triangles separates the nonpercolating region (on the left) from the percolating region (on the right) for model I. On the other

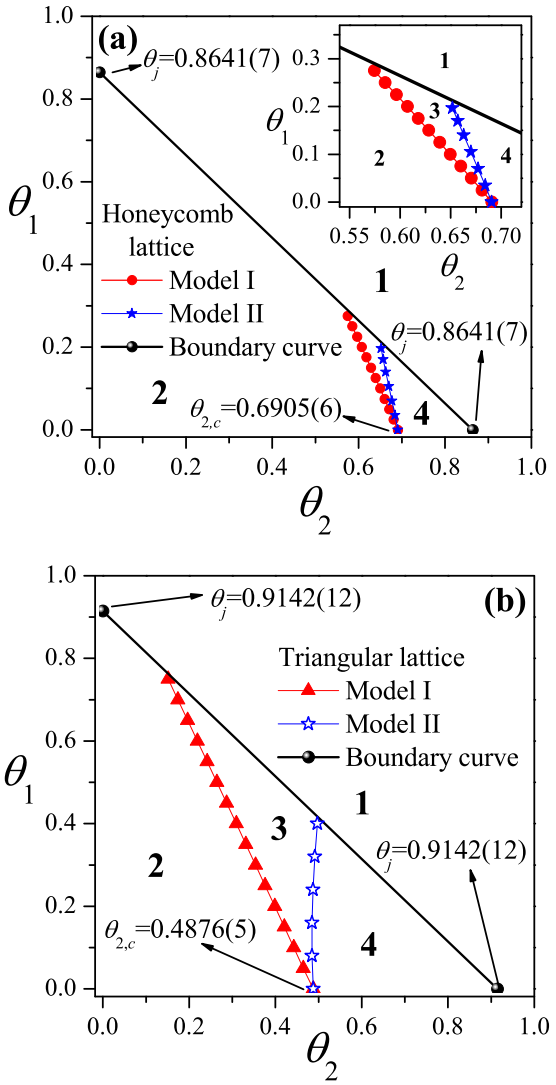


FIG. 4. (a) Percolation phase diagram corresponding to heteronuclear dimers on honeycomb lattices. Four regions can be distinguished. Region 1: forbidden region for models I and II; region 2: nonpercolating region for both models I and II; region 3: percolating region for model I and nonpercolating region for model II; and region 4: percolating region for models I and II. (b) Same as in part (a) for triangular lattices. As explained in the text, $\theta_1 = \theta_{AB}$ and $\theta_2 = \theta_{AA}$ for model I, and $\theta_1 = \theta_{BB}$ and $\theta_2 = \theta_{AA}$ for model II.

hand, the curve of open stars separates the nonpercolating region (on the left) from the percolating region (on the right) for model II. The values of $\theta_2 = \theta_{AA}$ remain approximately constant, and they do not depend on $\theta_1 = \theta_{BB}$ (note that in the case of honeycomb lattices the values of $\theta_2 = \theta_{AA}$ depend slightly on $\theta_1 = \theta_{BB}$.). Both curves begin at $\theta_2 = 0.4876(5)$, which is in concordance with the value of the percolation threshold for homogeneous dimers on triangular lattices [31]. Then, the percolation phase diagram splits into four regions, which have been labeled as 1, 2, 3, and 4. Region 1: forbidden region for models I and II; region 2: nonpercolating region for both models I and II; region 3: percolating region for model I and nonpercolating region for model II; and region 4: percolating region for models I and II.

Clearly, the obtained phase diagrams allow to determine how the different fractions of dimers $AA$, $AB$, and $BB$ affect the connectivity in both lattices and models. The present results can be compared with previous data for square lattices [27]. Even though the phase diagrams look similar for the three geometries (honeycomb $z = 3$, square $z = 4$, and triangular $z = 6$), some differences deserve to be highlighted: (a) the forbidden area for models I and II (region 1) decreases as the connectivity $z$ increases; (b) the percolating area for models I and II (region 4) increases as the connectivity increases; and (c) the nonpercolating area for models I and II (region 2) decreases as the connectivity increases. In summary, percolation is favored as the local connectivity is increased.

### B. Critical exponents and universality

In order to study the universality of the system, the critical exponents $\nu$, $\beta$, and $\gamma$ have been calculated. Knowing this set of exponents allows us a better understanding and characterization of the related problem.

The standard finite-size scaling theory [33] provides several ways to estimate the critical exponent $\nu$ from simulation data. One of this methods is from the maximum of the function $dR_L^X/d\theta_2$:

$$\left(\frac{dR_L^X}{d\theta_2}\right) \propto L^{1/\nu}. \tag{5}$$

In Fig. 5(a), $\log\left[(dR_L^X/d\theta_2)_{\max}\right]$ has been plotted as a function of $\log[L]$ for model I in honeycomb lattice and for model II in triangular lattice. According to Eq. (5), the slope of each line corresponds to $1/\nu$. As it can be observed, the slopes of the curves remain constant, being $\nu = 1.341(8)$ for model I in honeycomb lattice and $\nu = 1.335(4)$ for model II in triangular lattice.

Another alternative way for evaluating $\nu$ is from the divergence of the root mean square deviation of the percolation threshold observed from their average values $\Delta_L^X$:

$$\Delta_L^X \propto L^{-1/\nu}. \tag{6}$$

As an example of validity of Eq. (6), the inset in Fig. 5(a) shows $\Delta_L^A$ as a function of $L$ (note that both axes are in log-log scale) for the same cases of the main figure. According to Eq. (6), the slope of the line corresponds to $-1/\nu$. In this case, $\nu = 1.338(9)$ for model I in a honeycomb lattice and $\nu = 1.333(6)$ for model II in a triangular lattice. These results match, within numerical errors, with the exact value of the critical exponent of ordinary percolation $\nu = \frac{4}{3}$.

Once $\nu$ is known, the exponent $\gamma$ can be determined by scaling the maximum value of the susceptibility in Eq. (2) [36]. According to scaling assumptions, $\chi$ can be written as $\chi = L^{\gamma/\nu}\overline{\chi}(u)$, where $u = (\theta_2 - \theta_{2,c})L^{1/\nu}$ and $\overline{\chi}$ is the corresponding scaling function. At the point where $\chi$ is maximal, $u = \text{const}$ and $\chi_{\max} \propto L^{\gamma/\nu}$. Our simulation data for $\chi_{\max}$ are Fig. 5(b). The obtained values are $\gamma = 2.41(3)$ for model I in a honeycomb lattice and $\gamma = 2.40(2)$ for model II in a triangular lattice. Simulation data are consistent with the exact value of the critical exponent of ordinary percolation $\gamma = \frac{43}{18}$.

On the other hand, the exponent $\beta$ can be determined from the scaling behavior at criticality of the order parameter $P = L^{-\beta/\nu}\overline{P}(u')$, where $u' = |\theta_2 - \theta_{2,c}|L^{1/\nu}$ and $\overline{P}$ is the scaling

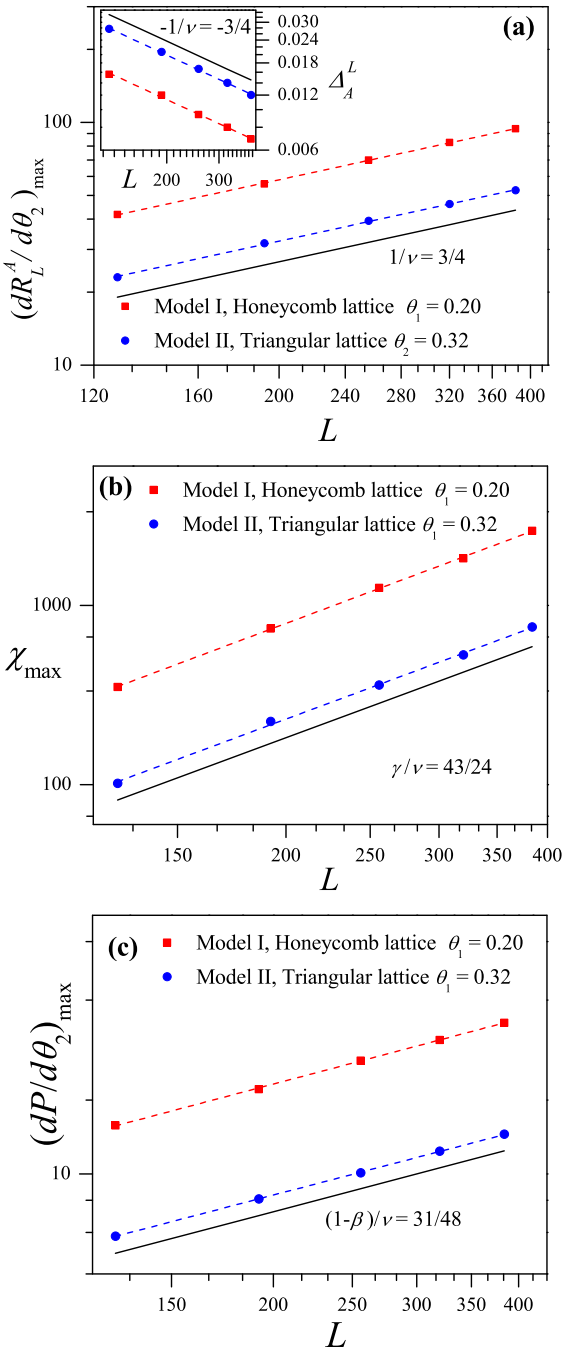


FIG. 5. (a) Maximum of the derivative of the $A$ percolation probability $(dR_L^A/d\theta_2)_{\max}$ as a function of $L$ (in a log-log scale) for two different cases: model I in honeycomb lattice (solid squares) and model II in triangular lattice (solid circles). Inset: standard deviation in Eq. (3) $\Delta_L^A$ as a function of $L$ (in a log-log scale) for the same cases shown in part (a). According to Eq. (6), the slope of each line corresponds to $-1/\nu = -\frac{3}{4}$. (b) Maximum of the susceptibility $\chi_{\max}$ as a function of $L$ (in a log-log scale) for the cases in part (a). The error bar in each measurement is smaller than the size of the symbols. The slope of each line corresponds to $\gamma/\nu = \frac{43}{24}$. (c) Maximum of the derivative of the percolation order parameter $(dP/d\theta_2)_{\max}$ as a function of $L$ (in a log-log scale) for the same cases reported in part (a). According to Eq. (7), the slope of each line corresponds to $(1-\beta)/\nu = \frac{31}{48}$.

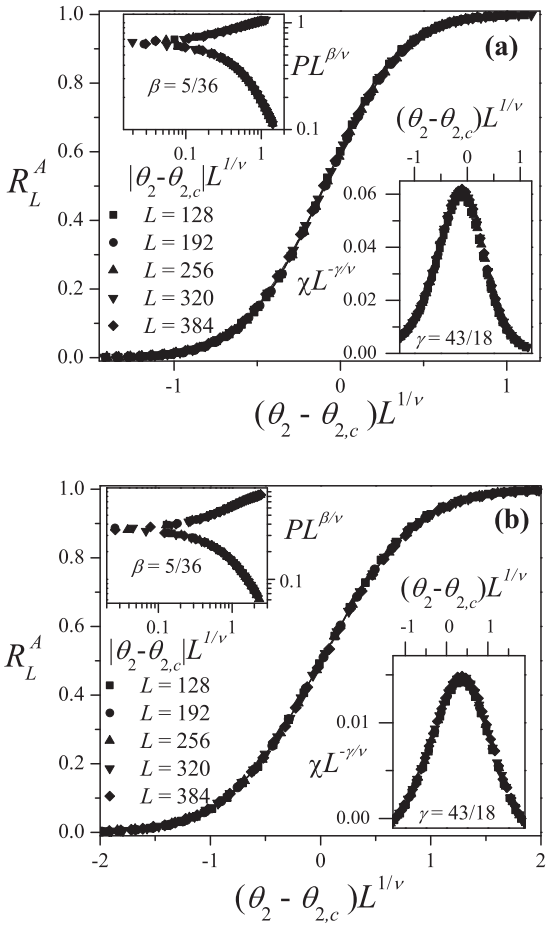


FIG. 6. Data collapsing of the percolation probability $R_L^A(\theta)$ vs $(\theta_2 - \theta_{2,c})L^{1/\nu}$. Upper left inset: data collapsing of the percolation order parameter $PL^{\beta/\nu}$ vs $|\theta_2 - \theta_{2,c}|L^{1/\nu}$. Bottom right inset: data collapsing of the susceptibility $\chi L^{-\gamma/\nu}$ vs $(\theta_2 - \theta_{2,c})L^{1/\nu}$. Two cases have been considered: (a) model I, honeycomb lattice, $\theta_1 = 0.20$; and (b) model II, triangular lattice, $\theta_1 = 0.32$.

function. At the point where $dP/d\theta_2$ is maximal, $u' = \text{const}$ and

$$\left(\frac{dP}{d\theta_2}\right)_{\max} = L^{(-\beta/\nu+1/\nu)}\overline{P}(u') \propto L^{(1-\beta)/\nu}. \tag{7}$$

The scaling of $(dP/d\theta_2)_{\max}$ is shown in the inset in Fig. 5(c) for same cases. From the slopes of the curves, the following values of $\beta$ were obtained: $\beta = 0.141(5)$ for model I in a honeycomb lattice and $\beta = 0.134(6)$ for model II in a triangular lattice. These results agree with the exact value of $\beta$ for ordinary percolation $\beta = \frac{5}{36}$.

The study of Fig. 5 was repeated for different values of the parameters of the system. In all cases, the values obtained for $\nu$ [Fig. 5(a)], $\gamma$ [Fig. 5(b)], and $\beta$ [Fig. 5(c)] clearly indicate that this problem belongs to the same universality class that the two-dimensional (2D) random percolation regardless the model (I or II) and the values of $\theta_{AA}, \theta_{AB}$, and $\theta_{BB}$ considered.

The scaling behavior has been tested by plotting $PL^{\beta/\nu}$ versus $|\theta_2 - \theta_{2,c}|L^{1/\nu}$, $\chi L^{-\gamma/\nu}$ versus $(\theta_2 - \theta_{2,c})L^{1/\nu}$, $R_L^A$ versus $(\theta_2 - \theta_{2,c})L^{1/\nu}$, and $U$ versus $(\theta_2 - \theta_{2,c})L^{1/\nu}$ and looking for data collapsing. Using the values of $\theta_{2,c}$ obtained and

the exact values of the critical exponents corresponding to ordinary percolation $\nu = \frac{4}{3}$, $\gamma = \frac{43}{18}$, and $\beta = \frac{5}{36}$, the curves have an excellent scaling collapse [see Figs. 6(a) and 6(b)]. This leads to independent controls and consistency checks of the values of all the critical exponents.

## IV. CONCLUSIONS

Irreversible deposition of defective dimers on honeycomb and triangular lattices was studied. The presence of defects in the dimers was analyzed. This was introduced as two kinds of segments composing the dimers: type $A$ (percolating) and type $B$ (nonpercolating). Thus, three types of dimers were considered: $AA$, $BB$, and $AB$.

In the filling process, two different models were analyzed, according to the types of dimers deposited on the lattice. In model I (II), $AB$ ($BB$) and $AA$ dimers were deposited up to a total coverage $\theta_T = \theta_{AB}$ ($\theta_{BB}$) $+ \theta_{AA}$ was reached. We initially fixed the value of $\theta_{AB}$ (model I) or $\theta_{BB}$ (model II) and, in a second stage, a fraction $\theta_{AA}$ of $AA$ dimers was deposited on the lattice. The connectivity analysis was carried out by accounting only for the conductive segments.

The percolation threshold was calculated for each geometry (triangular and honeycomb) and deposition mechanism (models I and II). Accordingly, the complete phase diagram separating the percolating from the nonpercolating regions was determined for each considered lattice and deposition model. Several conclusions can be drawn from this study and previous work for square lattices [27]:

(1) Four regions can be distinguished in each percolation phase diagram. Region 1: forbidden region for models I and II; region 2: nonpercolating region for both models I and II; region 3: percolating region for model I and nonpercolating region for model II; and region 4: percolating region for models I and II.

(2) The jamming coverage plays an important role in the system considered here. In fact, the curve $\theta_T = \theta_j$ determines the space of all the allowed values of $\theta_1$ and $\theta_2$ (regions 2, 3, and 4). $\theta_j = 0.90681(5)$ [43], 0.9142(12) [31], and 0.864(7) [32], for square, triangular, and honeycomb lattices, respectively.

(3) The curves separating regions 2-3-4 vary between the abscissa axis ($\theta_2$ axis) and the curve $\theta_T = \theta_j$. The intersection point with the $\theta_2$ axis determines the percolation threshold corresponding to homogeneous dimers: 0.564(2) [42], 0.4876(5) [31], and 0.6905(6) [42], for square, triangular, and honeycomb lattices, respectively.

Finally, the accurate determination of the critical exponents $\nu$, $\beta$, and $\gamma$ revealed that, regardless the geometry (triangular or honeycomb), the model (I or II) and the values of $\theta_{AA}$, $\theta_{AB}$, and $\theta_{BB}$ considered, the problem belongs to the same universality class as 2D random percolation model. An identical result was obtained in Ref. [27] for heteronuclear dimers on square lattices.

## ACKNOWLEDGMENTS

This work was supported in part by CONICET (Argentina) under Project No. PIP 112-201101-00615; Universidad Nacional de San Luis (Argentina) under Project No. 03-0816; and the National Agency of Scientific and Technological Promotion (Argentina) under Project No. PICT-2013-1678. The numerical work was done using the BACO parallel cluster (composed by 50 PCs each with an Intel i7-3370/2600 processor) located at Instituto de Física Aplicada, Universidad Nacional de San Luis-CONICET, San Luis, Argentina.

[1] J. Becklehimer and R. B. Pandey, Phys. A (Amsterdam) **187**, 71 (1992).
[2] Y. Leroyer and E. Pommiers, Phys. Rev. B **50**, 2795 (1994).
[3] B. Bonnier, M. Hontebeyrie, Y. Leroyer, C. Meyers, and E. Pommiers, Phys. Rev. E **49**, 305 (1994).
[4] N. Vandewalle, S. Galam, and M. Kramer, Eur. Phys. J. B **14**, 407 (2000).
[5] G. Kondrat and A. Pękalski, Phys. Rev. E **63**, 051108 (2001).
[6] V. Cornette, A. J. Ramirez-Pastor, and F. Nieto, Phys. Lett. A **353**, 452 (2006).
[7] V. Cornette, A. J. Ramirez-Pastor, and F. Nieto, J. Chem. Phys. **125**, 204702 (2006).
[8] N. I. Lebovka, N. N. Karmazina, Y. Y. Tarasevich, and V. V. Laptev, Phys. Rev. E **84**, 061603 (2011).
[9] Y. Y. Tarasevich, N. I. Lebovka, and V. V. Laptev, Phys. Rev. E **86**, 061116 (2012).
[10] P. Longone, P. M. Centres, and A. J. Ramirez-Pastor, Phys. Rev. E **85**, 011108 (2012).
[11] Lj. Budinski-Petković, I. Lončarević, M. Petković, Z. M. Jakšić, and S. B. Vrhovac, Phys. Rev. E **85**, 061117 (2012).
[12] G. D. Garcia, F. O. Sanchez-Varretti, P. M. Centres, and A. J. Ramirez-Pastor, Eur. J. Phys. B **86**, 403 (2013).
[13] Lj. Budinski-Petković, I. Lončarević, Z. M. Jakšić, and S. B. Vrhova, J. Stat. Mech. (2016) 053101.
[14] G. Kondrat, Z. Koza, and P. Brzeski, Phys. Rev. E **96**, 022154 (2017).
[15] Y. Y. Tarasevich, V. V. Laptev, A. S. Burmistrov, and N. I. Lebovka, J. Phys.: Conf. Ser. **955**, 012006 (2018).
[16] M. Dolz, F. Nieto, and A. J. Ramirez-Pastor, Eur. Phys. J. B **43**, 363 (2005).
[17] Y. Y. Tarasevich and V. A. Cherkasova, Eur. Phys. J. B **60**, 97 (2007).
[18] V. A. Cherkasova, Y. Y. Tarasevich, N. I. Lebovka, and N. V. Vygornitskii, Eur. Phys. J. B **74**, 205 (2010).
[19] C. S. Dias, N. A. M. Araujo, and A. Cadilhe, Phys. Rev. E **85**, 041120 (2012).
[20] R. M. Ziff, E. Gulari, and Y. Barshad, Phys. Rev. Lett. **56**, 2553 (1986), and references therein.
[21] C. T. Rettner and H. Stein, Phys. Rev. Lett. **59**, 2768 (1987).
[22] C. T. Rettner and C. B. Mullins, J. Chem. Phys. **94**, 1626 (1991).
[23] J. E. Davis, P. D. Nolan, S. G. Karseboom, and C. B. Mullins, J. Chem. Phys. **107**, 943 (1997).
[24] Z. Gao and Z. R. Yang, Phys. A (Amsterdam) **255**, 242 (1998).

[25] H. Harder, A. Bunde, and W. Dieterich, J. Chem. Phys. **85**, 4123 (1986).
[26] H. Holloway, Phys. Rev. B **37**, 874 (1988).
[27] M. C. Gimenez and A. J. Ramirez-Pastor, Phys. Rev. E **94**, 032129 (2016).
[28] P. M. Centres, A. J. Ramirez-Pastor, and M. C. Gimenez, Phys. Rev. E **96**, 062136 (2017).
[29] Y. Yu. Tarasevich, V. V. Laptev, N. V. Vygornitskii, and N. I. Lebovka, Phys. Rev. E **91**, 012109 (2015).
[30] P. N. Suding and R. M. Ziff, Phys. Rev. E **60**, 275 (1999).
[31] E. J. Perino, D. A. Matoz-Fernandez, P. M. Pasinetti, and A. J. Ramirez-Pastor, J. Stat. Mech. (2017) 073206.
[32] G. A. Iglesias-Panuska, P. M. Centres, and A. J. Ramirez-Pastor (unpublished).
[33] K. Binder, Rep. Prog. Phys. **60**, 487 (1997).
[34] F. Yonezawa, S. Sakamoto, and M. Hori, Phys. Rev. B **40**, 636 (1989).
[35] J. Hoshen and R. Kopelman, Phys. Rev. B **14**, 3438 (1976).
[36] D. Stauffer and A. Aharony, *Introduction to Percolation Theory* (Taylor & Francis, London, 1994).
[37] M. C. Giménez, F. Nieto, and A. J. Ramirez-Pastor, J. Phys. A: Math. Gen. **38**, 3253 (2005).
[38] M. C. Giménez, F. Nieto, and A. J. Ramirez-Pastor, J. Chem. Phys. **125**, 184707 (2006).
[39] S. Biswas, A. Kundu, and A. K. Chandra, Phys. Rev. E **83**, 021109 (2011).
[40] A. K. Chandra, Phys. Rev. E **85**, 021149 (2012).
[41] L. Kurzawski and K. Malarz, Rep. Math. Phys. **70**, 163 (2012).
[42] V. Cornette, A. J. Ramirez-Pastor, and F. Nieto, Phys. A (Amsterdam) **71**, 327 (2003).
[43] P. M. Centres and A. J. Ramirez-Pastor, J. Stat. Mech. (2015) P10011.